Geol Rundsch (1996) 85:577–585

ORIGINAL PAPER

A. Bollhöfer · A. Eisenhauer · N. Frank · D. Pech
A. Mangini

Thorium and uranium isotopes in a manganese nodule from the Peru basin determined by alpha spectrometry and thermal ionization mass spectrometry (TIMS): Are manganese supply and growth related to climate?

Received: 12 July 1995 / Accepted: 4 January 1996

Abstract Thorium- and uranium isotopes were measured in a diagenetic manganese nodule from the Peru basin applying alpha- and thermal ionization mass spectrometry (TIMS). Alpha-counting of 62 samples was carried out with a depth resolution of 0.4 mm to gain a high-resolution $^{230}Th_{excess}$ profile. In addition, 17 samples were measured with TIMS to obtain precise isotope concentrations and isotope ratios. We got values of 0.06–0.59 ppb (^{230}Th), 0.43-1.40 ppm (^{232}Th), 0.09–0.49 ppb (^{234}U) and 1.66–8.24 ppm (^{238}U). The uranium activity ratio in the uppermost samples (1–6 mm) and in two further sections in the nodule at 12.5 ± 1.0 mm and 27.3–33.5 mm comes close to the present ocean water value of 1.144 ± 0.004. In two other sections of the nodule, this ratio is significantly higher, probably reflecting incorporation of diagenetic uranium. The upper 25 mm section of the Mn nodule shows a relatively smooth exponential decrease in the $^{230}Th_{excess}$ concentration (TIMS). The slope of the best fit yields a growth rate of 110 mm/Ma up to 24.5 mm depth. The section from 25 to 30.3 mm depth shows constant $^{230}Th_{excess}$ concentrations probably due to growth rates even faster than those in the top section of the nodule. From 33 to 50 mm depth, the growth rate is approximately 60 mm/Ma. Two layers in the nodule with distinct laminations (11–15 and 28–33 mm depth) probably formed during the transition from isotopic stage 8 to 7 and in stage 5e, respectively. The Mn/Fe ratio shows higher values during interglacials 5 and 7, and lower ones during glacials 4 and 6. A comparison of our data with data from adjacent sediment cores suggests (a) a variable supply of hydrothermal Mn to sediments and Mn nodules of the Peru basin or (b) suboxic conditions at the water sediment interface during periods with lower Mn/Fe ratios.

Key words Manganese nodules · Thorium dating · Uranium isotopes · Peru basin · TIMS

A. Bollhöfer (✉) · A. Eisenhauer · N. Frank · D. Pech
A. Mangini
Heidelberger Akademie der Wissenschaften, c/o Institut für Umweltphysik, INF 366, D-69120 Heidelberg, Germany
Fax: +06221/546405
e-mail: bo@uphys1.uphys.uni-heidelberg.de

Introduction

The uncertainty of how post-depositional migration of Mn may have altered the original distribution in the sediments makes the record of Mn (or Mn/Fe) in deep sea sediments a questionable proxy for changes of the water column chemistry. The advantages in studying diagenetic Mn nodules are that the record of Mn cannot be superimposed by post-depositional remobilization, and dating of diagenetic manganese nodules allows a time resolution at least one order of magnitude better than for hydrogenetic crusts.

Hydrothermalism is probably the major source of manganese to the oceans. One may estimate the flux of manganese from the mid-ocean ridges to 5×10^6 tons/a, assuming the flux of seawater through the ridges to be $(1.5 \pm 0.4) \cdot 10^{14}$ kg/a and an average Mn content of hydrothermal solutions of 600 μmol/kg (Holland 1984). The flux of detrital Mn ranges between 1 and $2 \cdot 10^6$ tons/a, assuming an average sedimentation rate of detrital clays of 0.2 cm/ka with an average Mn content of 6000 ppm (Bischoff et al. 1979). Thus, the detrital Mn supply is smaller than the hydrothermal. Due to the different sources of Mn in the ocean, there are different suppliers of Mn to diagenetic nodules (Lyle et al. 1979; Leinen and Pisias 1984).

Under present-day conditions, hydrothermal Mn precipitates close to its sources due to its residence time in the water column of approximately 50 years. The horizontal propagation distance for hydrothermal Mn in the water column is thus estimated to be in the order of 1000 km (Weiss 1977). This order of magnitude for

propagation of hydrothermal Mn is corroborated by multifactor analysis on cores from a transect from the EPR to New Zealand at 42°S (Schmitz 1985).

The influence of Mn of hydrothermal origin in sediments within some distance from the sources is reflected clearly by Mn/Al ratios in excess of 0.06, the average ratio observed in pelagic sediments with a negligible hydrothermal component (Chester and Aston 1976). Excess Mn was observed, for example, in sediment cores from the MANOP site H (Finney et al. 1988), from the Central and Northern Peru basin (Stoffers et al. 1984), along the East Pacific rise (Walter and Stoffers 1985) and from the Galapagos microplate (Mangini et al. 1994), suggesting additional supply of Mn of hydrothermal origin to these areas during the Late Quaternary. The depth profiles of Mn/Fe in cores from these localities show a marked variability during the past several hundred thousands of years. This variability can be interpreted either as (a) a result of diagenetic mobilization of Mn in the sediments which eventually builds up peaks at the redoxcline (Berger et al. 1983; Finney et al. 1988) or (b) variations in the manganese or iron fluxes from the water column into the sediment (Mangini et al. 1994). The diagenetic processes are thought to be influenced by the flux of organic carbon to the sediments and thus the primary productivity, the sedimentation rate or the oxygen content of bottom water. Suboxic conditions in the sediments lead to a reduction of Mn(IV)oxide and to an upward diffusion of dissolved Mn(II) ions. At the oxic–anoxic interface where a higher redox potential prevails the Mn^{2+} reprecipitates as Mn(IV) oxide (Boudreau and Scott 1978; Froelich et al. 1979; Lyle 1981; Stackelberg 1988).The free energy-competition model suggests that reduction of Fe oxide to mobile Fe^{2+} occurs after reduction of Mn oxide (Berner 1980).

Growth conditions of Mn nodules in the Peru basin are determined mainly by diagenetic mobilization of Mn from the sediments. They are characterized by Mn/Fe ratios $\geqslant 5$, and may be classified as a diagenetic type. The large "cauliflower-like" nodules display microlayers several millimeters thick, rich in Mn, consisting of 10 Å-manganate (Halbach and Puteanus 1988). Growth rates of up to 170 mm/Ma were determined (Reyss et al. 1982; Finney et al. 1984). The growth rates of these diagenetic nodules are much faster than those of hydrogenetic ferromanganese encrustations from the Central Pacific in which Mn is supplied only from the water column (ca. 5 mm/Ma; Segl et al. 1989; Puteanus et al. 1989; Mangini et al. 1990; Eisenhauer et al. 1992). Manganese mass balances in diagenetic Mn nodules suggested that Mn and Fe were accreted also from bottom waters enriched in dissolved and particulate metal contents derived from areas remote from the site of nodule formation (Calvert and Piper 1984).

In our study we have determined the growth rate and the variability of Mn/Fe with time of a manganese nodule from station 63KG in the Peru basin. Our purpose was to derive a record of climatically controlled changes of Mn and/or Fe of bottom water in the Peru basin in the past. We compare the Mn/Fe profile of the nodule with records from adjacent sediments to check if the sediments records are primary or not.

Materials and methods

Station 63KG is located at 90°42′W and 6°45′S in the Peru basin ("Tiefsee-Umweltschutz-Programm" area; Fig. 1). The nodule was sampled with a box corer in a water depth of 4257 m during SONNE 79 cruise in 1992. It has a cauliflower, ellipsoidal shape, a diameter of approximately 10 cm and shows distinct laminations (Fig. 2). Darker layers with a more solid texture (up to 5 mm thick) alternate with dark-brown amorphous laminae with a higher porosity including very fine sedimentary debris.

For better handling the nodule was embedded in gypsum and fixed in a sample holder. Two profiles

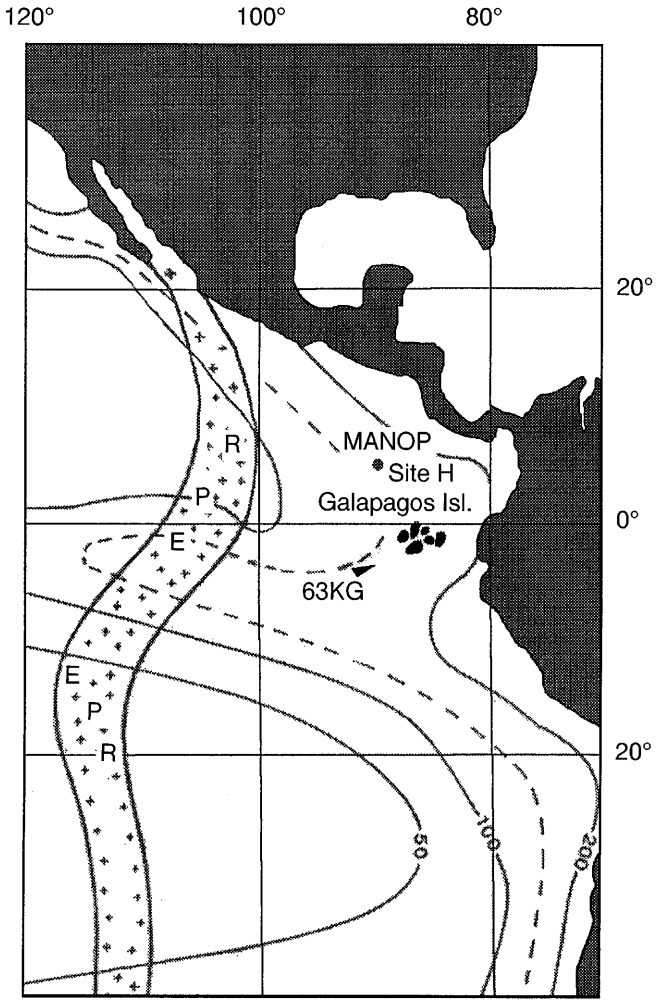

Fig. 1 Location of nodule 63KG located at 6°45′S, 90°42′W in a water depth of 4257 m. In addition, MANOP site H (*circle*) and the Galapagos Islands (*black dots*) are marked. The isolines mark the primary biological productivity in surface waters in g C m^{-2} $year^{-1}$ (Halbach et al. 1988)

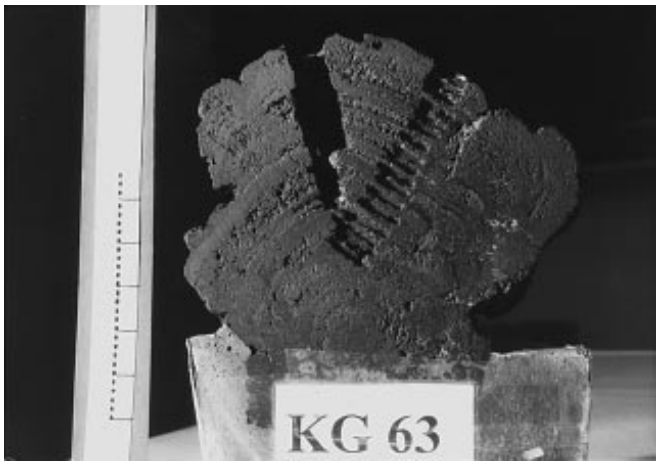

Fig. 2 Nodule 63KG. One can see the significant lamination and the two profiles that were taken for the α (left) measurements and the thermal ionization mass spectrometry (TIMS; right) measurements, respectively. Height of nodule ca. 7 cm

were drilled with a numerically controlled milling machine. For the TIMS measurements of ^{238}U, ^{234}U, ^{232}Th and ^{230}Th we took samples approximately every 3 mm from the surface to 50 mm depth at a depth resolution of 1–2.6 mm. The second profile was taken continuously to 24.4 mm depth at a depth resolution of 0.4 mm for the standard α-counting. Atomic absorption spectrometry (AAS) measurements of manganese and iron were also performed on the second profile.

For the TIMS analysis of uranium, we used a ^{233}U/^{236}U double spike to correct for instrumental fractionation. The concentration of the spike was calibrated against the 112A uranium standard material (New Brunswick Laboratories, New Brunswick, New Jersey). The mean of the ^{234}U/^{238}U ratio of 11 measurements of the 112A material yielded a value of $(5.3007 \pm 0.0060) \cdot 10^{-5}$ leading to a δ-uranium of (-31.3 ± 1.1). This value agrees well with those published previously by Edwards et al. (1993).

For thorium measurements we used a ^{229}Th spike calibrated against a ^{232}Th standard of well-known concentration. Cross-checks with standard material from other laboratories (Gif-sur-Yvette and Caltech) revealed good agreement within the statistical uncertainty ($\pm 0.6\%$). The measurements were performed with a Finnigan MAT262 RPQ mass spectrometer, in peak jumping mode, using the secondary electron multiplier and the double filament technique. The analytical and measurement procedures follow closely those described previously by Chen et al. (1986), Edwards et al. (1987) and Chabaux et al. (1995). Chemical yields are approximately 60–80% for thorium and approximately 90% for uranium.

The analytical procedure for the α-spectrometry is similar to that described by Ku and Broecker (1967), Krishnaswami et al. (1982) and Mangini et al. (1988). Counting time for the α-measurement of ^{230}Th was approximately 2 days, resulting in a statistical uncertainty of approximately 15%.

Results

The results of the TIMS measurements are presented in Table 1. The data are given in decay events per minute per gram (dpm/g). The ^{230}Th activity in the nodule is plotted as a function of depth in Fig. 3. The values obtained with the two methods (α and TIMS) agree well over the whole section from 0 to 25 mm. Although the two profiles were drilled at different locations of the nodule, the ^{230}Th concentration shows a good spatial

Table 1 Results of the ^{238}U, ^{234}U, ^{232}Th and ^{230}Th measurements by Thermal Ionization Mass Spectrometry (TIMS). For convenience of comparison the data are given in dpm/g

Depth (mm)	Th-230 (dpm/g)	Th-232 (dpm/g)	U-234 (dpm/g)	U-238 (dpm/g)	Activity ratio (U-234/U-238)	Th-230 excess (dpm/g)
1.0 ± 1.0	26.90 ± 0.338	0.341 ± 0.002	2.263 ± 0.064	1.989 ± 0.016	1.138 ± 0.033	26.30 ± 0.334
3.5 ± 0.5	21.29 ± 0.360	0.321 ± 0.003	3.856 ± 0.076	3.412 ± 0.027	1.130 ± 0.024	20.04 ± 0.272
6.0 ± 1.0	20.03 ± 0.380	0.257 ± 0.003	6.778 ± 0.132	6.147 ± 0.057	1.103 ± 0.024	17.03 ± 0.198
9.5 ± 1.0	12.68 ± 0.254	0.228 ± 0.001	4.468 ± 0.116	3.856 ± 0.039	1.159 ± 0.032	10.34 ± 0.213
12.5 ± 1.0	11.40 ± 0.151	0.221 ± 0.002	4.553 ± 0.055	4.084 ± 0.028	1.115 ± 0.016	8.765 ± 0.123
15.0 ± 1.0	9.194 ± 0.364	0.249 ± 0.004	2.013 ± 0.091	1.664 ± 0.019	1.210 ± 0.056	7.878 ± 0.321
18.3 ± 1.3	7.825 ± 0.183	0.187 ± 0.001	3.712 ± 0.054	3.268 ± 0.017	1.136 ± 0.018	5.275 ± 0.128
21.8 ± 1.3	5.836 ± 0.252	0.163 ± 0.001	3.087 ± 0.074	2.761 ± 0.018	1.118 ± 0.028	3.625 ± 0.161
24.5 ± 1.0	6.055 ± 0.177	0.156 ± 0.002	2.886 ± 0.151	2.198 ± 0.026	1.313 ± 0.070	3.898 ± 0.118
27.3 ± 0.8	6.597 ± 0.070	0.203 ± 0.001	2.317 ± 0.051	2.156 ± 0.022	1.074 ± 0.026	4.786 ± 0.060
30.3 ± 0.8	5.446 ± 0.257	0.105 ± 0.002	3.879 ± 0.072	3.641 ± 0.044	1.065 ± 0.024	2.346 ± 0.113
33.5 ± 1.0	12.87 ± 0.895	0.330 ± 0.017	3.395 ± 0.050	3.228 ± 0.028	1.052 ± 0.018	9.887 ± 0.704
37.3 ± 1.3	6.434 ± 0.113	0.315 ± 0.002	2.001 ± 0.035	1.781 ± 0.007	1.124 ± 0.020	4.595 ± 0.096
40.5 ± 1.0	4.347 ± 0.150	0.158 ± 0.002	3.103 ± 0.109	2.997 ± 0.027	1.035 ± 0.037	1.440 ± 0.115
43.3 ± 1.3	4.054 ± 0.048	0.134 ± 0.001	1.749 ± 0.026	1.683 ± 0.009	1.039 ± 0.016	2.372 ± 0.098
46.3 ± 0.8	3.946 ± 0.108	0.141 ± 0.002	3.471 ± 0.078	3.218 ± 0.043	1.078 ± 0.028	0.571 ± 0.017
40.9 ± 1.0	2.730 ± 0.047	0.158 ± 0.002	1.297 ± 0.031	1.242 ± 0.013	1.044 ± 0.027	1.460 ± 0.043

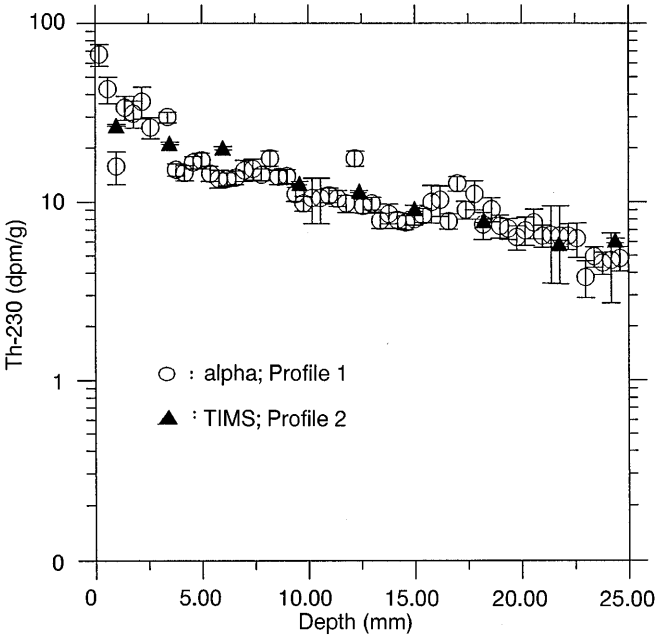

Fig. 3 ^{230}Th (α- and TIMS data) plotted vs depth from 0–25 mm. The decreasing trend with depth is superimposed by frequent oscillations of the ^{230}Th concentration. The α- and TIMS values are in general accord within the statistical uncertainties (1σ for the α measurements; 2σ for TIMS). Although the two profiles were drilled at different localities of the nodule, the ^{230}Th concentration shows a good spatial homogeneity

homogeneity. For calculating the $^{230}Th_{excess}$ concentrations we applied:

$$^{230}Th_{xs} = {}^{230}Th_{total} - 0.7 \cdot {}^{232}Th_{total} - 1.144 \cdot ({}^{238}U_{total} - 0.7 \cdot {}^{232}Th_{total}) \cdot (1 - e^{-\lambda t}) \quad (1)$$

where $\lambda = 9.195 \cdot 10^{-6}$ year^{-1}.

The first term in this equation is the total measured ^{230}Th activity. The second term describes the detrital part of ^{230}Th, with 0.7 being the mean value of the ^{238}U/^{232}Th ratio of eight sediment cores from the Peru basin under the assumption that the detrital ^{230}Th component is in radioactive equilibrium with the detrital ^{238}U (see Table 2). The third term takes into account the decay of uranium incorporated into the nodule from the water column. Equation (1) can be solved iteratively by fitting the experimental data.

Growth rates

The concentration of $^{230}Th_{excess}$ is approximately 14.8–66.3 dpm/g in the surface samples (0–1 mm, α-data; Table 3) and decreases towards the interior of the nodule to 0.57 dpm/g at 46.25 mm depth (TIMS). The surface concentration is up to 50 times lower than that in the surface of hydrogenetic samples because of the higher flux of manganese into the nodule.

To determine the growth rates, we used the standard technique described by Mangini et al. (1988) and Eisenhauer et al. (1992). $^{230}Th_{excess}$ TIMS plotted against depth (up to 50 mm; Fig. 4) allows to distinguish three sections with different growth rates. From the surface to approximately 25 mm depth, the smooth decrease in the $^{230}Th_{excess}$ activity yields a growth rate of 110 mm per million years. From 25 to approximately 30.3 mm depth, constant activities probably reflect a period of very fast growth. From 33 mm depth to the end of the profile at 50 mm, the steeper slope of $^{230}Th_{excess}$ suggests a growth rate of approximately 60 mm per million years.

Due to our assumption of different sources of ^{232}Th (detrital introduced by rivers and aeolian dust) and $^{230}Th_{excess}$ (hydrogeneous, from the decay of dissolved uranium in the water column) in diagenetic nodules (Huh and Ku 1984), we did not calculate the growth rates using the $^{230}Th_{excess}/^{232}$Th normalizing technique.

The flux of $^{230}Th_{excess}$ was calculated with a mean growth rate of 110 mm/Ma, a dry bulk density of approximately 1.5 g/cm^3 and a surface concentration of 27 dpm/g as calculated from the best-fit line (Fig. 4). It amounts to 0.47 dpm/cm^2/ka, which is only 2.5% of the flux into adjacent sediments of the Peru basin (Ta-

Table 2 ^{238}U/^{232}Th activity ratios, sedimentation rates and $^{230}Th_{excess}$ fluxes [dpm/cm^2/ka] of 8 sediment cores from the Peru Basin. The fluxes into cores 1–7 were calculated with a mean dry bulk density of 0.25 g/cm^3. The flux into core 9KL, which is located nearest to nodule 63 KG (90°42′W, 6°45′S), was calculated with the measured dry bulk densities. The flux of 0.47 dpm/cm^2/ka into nodule 63KG is only about 2.5 percent of the flux into sediment core 9KL

Number	Designation	Location	^{238}U/^{232}Th activity ratio	Sedimentation rate (cm/ka)	$^{230}Th_{excess}$ flux (dpm/cm^2 per ka)
1	108KL	90°39′W, 7°02′S	0.71	0.36	16.5
2	106KG	90°39′W, 7°02′S	0.88	1.10	14.3
3	77KL	90°28′W, 6°34′S	0.57	1.19	16.4
4	9KL	90°28′W, 6°34′S 90°46′W, 6°43′S	0.7	0.86	18.5
5	169KL	90°50′W, 8°10′S	0.63	0.18	7.2
6	170KG	90°50′W, 8°10′S	0.51	0.26	7.7
7	25KG	90°26′W, 6°52′S	0.63	0.37	7.5
8	26KL	90°27′W, 6°52′S	0.68	0.24	4.4

Table 3 Data of the alpha and AAS measurements, partial accumulation rates (CF-rate) and ages (CF-age) as calculated with the constant flux model, using a flux of 4.7 dpm/mm^2/Ma, a mean dry bulk density of 1.5 mg/mm^3 (ρ) and the time corrected $^{230}Th_{excess}$ values: $^{230}Th_{excess}corr = {}^{230}Th_{excess} \cdot e^{\lambda t}$. CF-rate[mm/Ma] = (Flux)/($^{230}Th_{excess}corr \cdot \rho$)·1000; CF-age[a] = depth[mm]/CF-rate·10^6.

No.	Depth (mm)	^{230}Th (dpm/g)	±	^{234}U (dpm/g)	±	$^{230}Th_{excess}$ (dpm/g)	±	CF rate (mm/Ma)	±	CF age (a)	Age[a] (a)	Mn (%)	±	Fe (%)	±
1	0.2	66.6	9.1	6.8	3.0	66.3	9.3	45	6	4409	1818				
2	0.6	42.8	7.2	6.8	3.0	42.1	7.5	67	12	11814	5455				
3	1	15.7	3.3	6.8	3.0	14.8	3.8	183	46	15905	9091				
4	1.4	34.0	5.3	6.8	3.0	32.8	5.8	80	14	19509	12727				
5	1.8	31.3	5.4	6.8	3.0	29.9	6.0	84	17	24407	16364				
6	2.2	36.6	7.3	6.8	3.0	35.0	8.1	68	16	29734	20000				
7	2.6	26.2	3.6	6.8	3.0	24.4	4.5	93	17	34811	23636				
8	3	131.4	7.4	6.4	0.9	129.0	7.7	15	1	49990	27273	29.07	0.51	0.36	0.03
9	3.4	29.9	2.1	5.2	0.7	27.5	2.4	62	5	66258	30909	49.84	0.83	0.65	0.01
10	3.8	15.1	1.2	3.8	0.5	13.3	1.5	123	13	71116	34545	43.08	0.72	0.29	0.01
11	4.2	14.5	1.4	4.6	0.7	12.2	1.8	129	19	74294	38182	39.67	0.75	0.34	0.02
12	4.6	16.6	1.3	6.1	0.7	13.5	1.7	114	14	77604	41818	39.36	0.94	0.39	0.01
13	5	17.0	1.8	8.4	0.9	12.6	2.3	118	21	81059	45455	40.49	0.91	0.45	0.01
14	5.4	14.4	1.5	8.2	1.0	10.0	2.1	145	29	84134	49091	38.04	0.86	0.42	0.01
15	5.8	13.5	1.5	8.3	1.0	8.9	2.1	158	37	86779	52727	27.49	0.49	0.35	0.01
16	6.2	13.4	1.1	9.1	1.2	8.3	1.9	166	36	89243	56364	36.61	0.61	0.29	0.01
17	6.6	13.7	1.2	7.8	1.0	9.2	1.8	146	28	91816	60000	41.64	0.84	0.32	0.01
18	7	15.0	2.0	4.1	0.7	12.7	2.4	103	20	95125	63636	35.22	0.71	0.33	0.01
19	7.4	15.3	2.0	6.1	0.9	11.7	2.6	108	24	98912	67273	39.91	1.18	0.45	0.01
20	7.8	14.2	1.1	6.8	0.9	10.0	1.8	122	21	102406	70909	42.73	0.76	0.45	0.01
21	8.2	17.5	1.7	7.2	0.8	13.0	2.2	91	15	106257	74545	41.80	0.97	0.46	0.01
22	8.6	13.8	1.3	8.8	1.0	8.1	1.9	140	32	109888	78182	41.94	1.14	0.35	0.01
23	9	13.9	1.2	6.7	0.8	9.6	1.8	116	21	113039	81818	42.93	1.03	0.40	0.01
24	9.4	11.1	1.0	7.4	0.8	6.2	1.6	174	43	115913	85455	43.07	1.03	0.30	0.01
25	9.8	9.8	0.9	8.0	0.8	4.5	1.5	238	80	117903	89091	44.71	1.04	0.33	0.01
26	10.2	10.5	3.0	7.9	1.8	5.3	4.3	198	159	119754	92727	40.78	0.82	0.25	0.01
27	10.6	10.5	3.0	5.0	0.6	7.1	3.5	143	69	122165	96364	43.06	0.76	0.26	0.01
28	11	10.9	1.0	6.3	1.1	6.6	1.8	150	40	124896	100000	40.56	0.69	0.25	0.01
29	11.4	10.4	1.1	7.3	1.0	5.4	1.9	181	60	127330	103636	39.67	0.68	0.26	0.01
30	11.8	9.8	1.1	5.1	0.6	6.2	1.5	152	36	129747	107273	43.03	0.87	0.30	0.01
31	12.2	17.5	1.7	3.6	0.4	14.9	2.1	61	8	134334	110909	42.87	0.93	0.31	0.01
32	12.6	9.5	0.9	5.0	0.6	5.8	1.4	150	34	138944	114545	41.66	0.64	0.30	0.01
33	13	9.8	0.8	5.9	0.8	5.5	1.4	155	38	141572	118182	43.64	1.23	0.35	0.01
34	13.4	7.9	0.8	4.2	0.6	4.8	1.3	175	45	144005	121818	44.76	0.97	0.31	0.01
35	13.8	8.6	1.1	6.4	0.8	3.9	1.7	213	93	146089	125455	41.00	0.70	0.27	0.01
36	14.2	7.9	0.8	5.7	0.5	3.7	1.3	218	72	147945	129091	36.10	1.11	0.23	0.01
37	14.6	7.6	0.7	4.8	0.5	4.1	1.1	195	50	149889	132727	44.80	0.90	0.33	0.01
38	15	8.0	0.6	4.5	0.6	4.6	1.1	168	38	152109	136364	43.80	1.12	0.31	0.01
39	15.4	8.4	0.7	4.7	0.7	4.8	1.3	157	42	154570	140000	39.88	0.68	0.36	0.01
40	15.8	10.0	2.3	3.7	0.5	7.1	2.8	103	40	157775	143636	42.30	0.80	0.36	0.01
41	16.2	10.3	2.0	4.5	0.8	6.8	2.7	104	40	161635	147273	43.14	1.52	0.43	0.01
42	16.6	7.8	0.7	3.4	0.5	5.1	1.2	134	30	165055	150909	41.94	0.94	0.37	0.01
43	17	12.6	1.1	2.8	2.0	10.4	2.8	63	16	169717	154545	41.35	0.84	0.40	0.01
44	17.4	9.0	1.0	2.1	0.5	7.3	1.5	86	17	175215	158182	42.04	1.15	0.46	0.01
45	17.8	11.0	2.1	6.7	1.2	5.7	3.1	106	57	179426	161818	41.64	0.78	0.63	0.03
46	18.2	7.4	1.3	2.3	0.5	5.5	1.7	105	32	183208	165455	40.32	0.83	0.63	0.01
47	18.6	9.1	1.4	3.2	0.7	6.5	2.0	86	26	187436	169091	40.03	0.97	0.54	0.01
48	19	7.3	1.1	4.7	1.2	3.5	2.1	157	94	191037	172727	43.20	0.87	0.43	0.01
49	19.4	7.1	1.0	5.4	1.2	2.7	2.1	199	149	193319	176364	44.76	0.75	0.38	0.02
50	19.8	6.3	1.0	3.8	0.7	3.2	1.6	162	80	195556	180000	43.50	0.71	0.25	0.01
51	20.2	6.9	1.3	3.5	0.7	4.0	1.9	127	59	198358	183636	39.29	1.21	0.24	0.01
52	20.6	7.6	1.4	4.1	2.0	4.2	3.3	117	88	201631	187273	42.15	1.04	0.33	0.01
53	21	6.5	0.9	4.7	0.8	2.5	1.7	191	123	204380	190909	39.66	0.61	0.28	0.01
54	21.4	6.5	3.0	3.3	1.0	3.7	3.9	127	132	206998	194545	43.95	0.78	0.27	0.02
55	21.8	6.5	3.0	4.6	1.6	2.5	4.5	179	308	209688	198182	40.98	0.72	0.25	0.01
56	22.2	6.5	1.1	3.2	0.7	3.8	1.7	118	52	212495	201818	42.52	0.66	0.23	0.01
57	22.6	6.2	1.4	2.9	2.0	3.7	3.2	116	98	215902	205455	45.28	0.70	0.32	0.01
58	23	3.8	0.9	2.7	0.7	1.4	1.5	298	308	218290	209091	32.13	0.88	0.15	0.01
59	23.4	4.9	0.6	3.6	0.6	1.8	1.2	229	144	219834	212727	34.31	0.52	0.18	0.01
60	23.8	4.6	0.7	2.8	0.5	2.1	1.2	196	106	221730	216364	37.71	0.63	0.20	0.01
61	24.2	4.7	2.0	2.8	0.4	2.2	2.4	179	191	223871	220000	15.86	0.26	0.07	0.01
62	24.6	4.8	0.8	3.7	0.6	1.6	1.3	241	186	225821	223636	50.08	1.49	0.32	0.01

[a] Age calculated with a constant mean accumulation rate of 110 mm/Ma (TIMS)

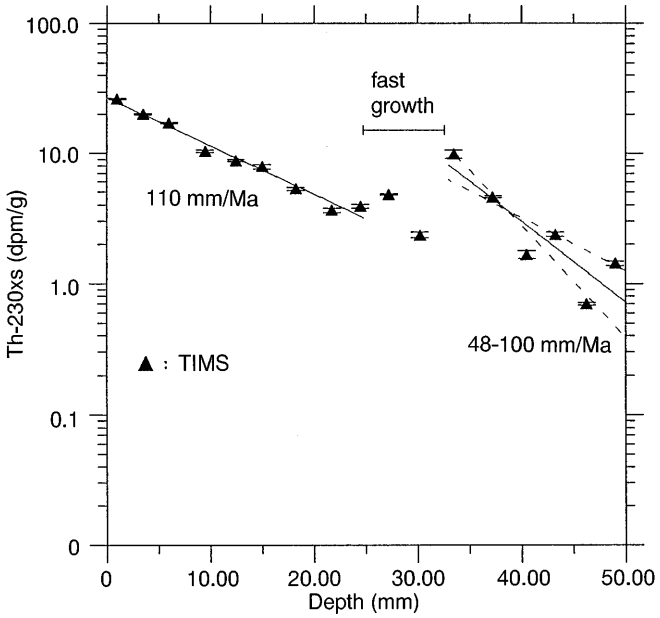

Fig. 4 $^{230}Th_{excess}$ (TIMS data) plotted vs depth from 0–50 mm. One can distinguish three different sections of growth

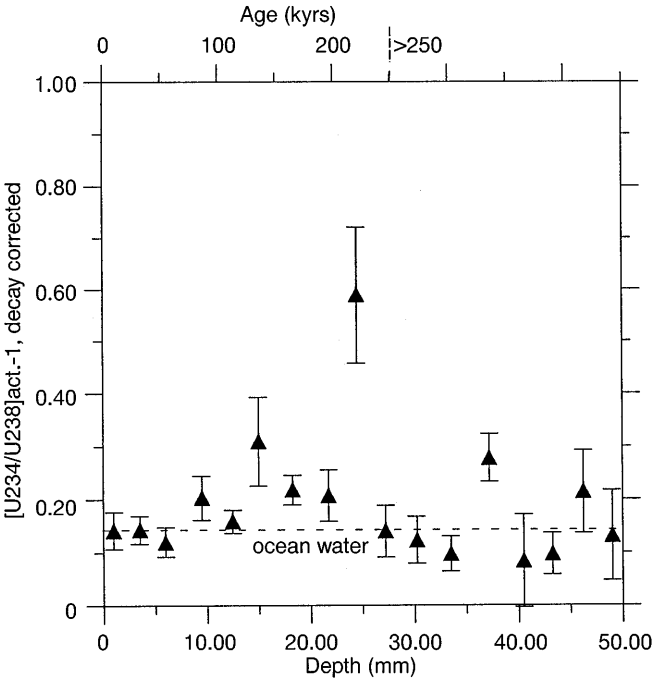

Fig. 5 $^{234}U/^{238}U$ activity ratio minus 1 (2σ; TIMS) plotted vs depth and age, respectively. The *dashed line* marks the value of the present ocean water of 1.144 ± 0.004

ble 2). The flux into the nodule is between one half and one fifth of the flux into two hydrogenetic encrustations from the North Equatorial Pacific (Eisenhauer et al. 1992).

There are two outstanding dark layers in the nodule in 11–15 and 28–33 mm depth, characterized by a more solid texture, composed of microlaminae and displaying a lower porosity. According to our calculated growth rates these two layers have grown close to the transition from glacial stage 8 to interglacial 7 during the period of fast growth, and from 136 to approximately 100 ka before present (stage 5e), respectively. Therefore, both layers seem to have formed during periods of drastic climatic change. However, in the upper 25 mm of the nodule several other changes in the internal structure of smaller magnitude than the two major changes can be seen, which cannot be as easily related to climatic events.

Uranium activity ratio

The decay-corrected uranium activity ratio (Fig. 5) of the three topmost samples (1–6 mm) and two other sections of the nodule (12.5 ± 1 and 27.3–33.5 mm), including the two dark layers, comes close to the present ocean water value of 1.144 ± 0.004 (Chen et al. 1986) mirroring incorporation of hydrogenetic uranium. In two other sections (15–24.5 and 37.3 ± 1.3 mm), this ratio significantly exceeds the present ocean water value probably due to incorporation of diagenetic uranium. In making this assumption we imply a closed system behaviour and no post-depositional migration of uranium within the manganese encrustation (Chabaux 1995).

The decay-corrected activity ratios vary from 1.035 (40.5 mm) to 1.313 (24.5 mm) with a mean value of 1.114. Future work aims to measure this ratio with a higher accuracy.

Manganese and iron in Nodule 63KG

The manganese concentration varies between 30 and 50% with a mean value of approximately 40% The iron content between 0.2 and 0.6% displays a significantly larger variability than manganese (Table 3). This is also the case for the ratio of Mn/Fe with ratios between 63 and 213. The flux of Mn of $6.6 \cdot 10^{-3}$ g/cm^2 per ka (11 cm/Ma · 0.4 g/g · 1.5 g/cm^3) is comparable to the flux into sediments of the Central and Northern Peru basin (Stoffers et al. 1984), whereas the flux of Fe is several orders of magnitude smaller. These higher Mn concentrations and fluxes into the nodule accentuate the diagenetic origin of nodule 63 KG.

After transforming our depth scale into a time scale, applying the growth rates derived from the TIMS measurements, the profile of Mn/Fe in the nodule (Fig. 6) shows low ratios in samples from glacial stages 4, 6 and probably 8, and higher ones in interglacial stages 5 and 7 suggesting either an enhanced iron flux or a smaller manganese flux into the nodule during glacials. The latter is more probable because the decay-corrected $^{230}Th_{excess}$ (Fig. 7) shows higher concentrations during glacial 4 and specially during glacial 6. Assuming a constant flux of ^{230}Th into the nodule, the maxima of

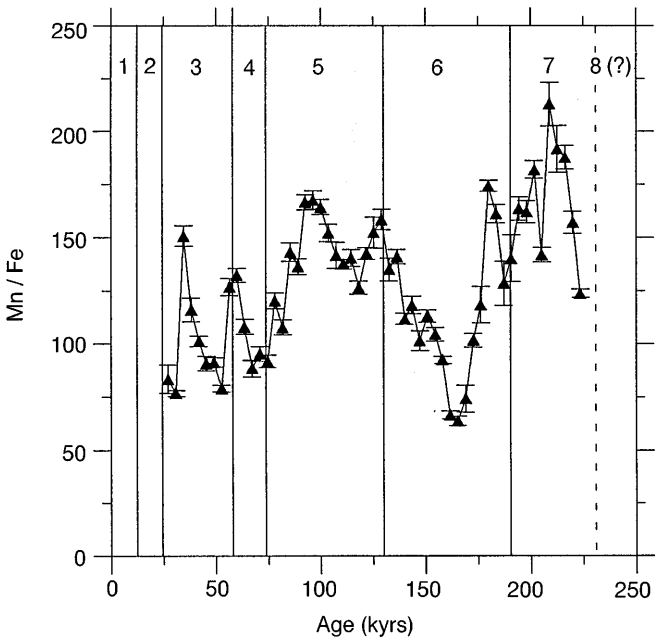

Fig. 6 Mn/Fe ratio of nodule 63KG vs the age calculated with a growth rate of 110 mm/Ma. The *vertical lines* represent the transitions of the isotopic stages following Martinson et al. (1987)

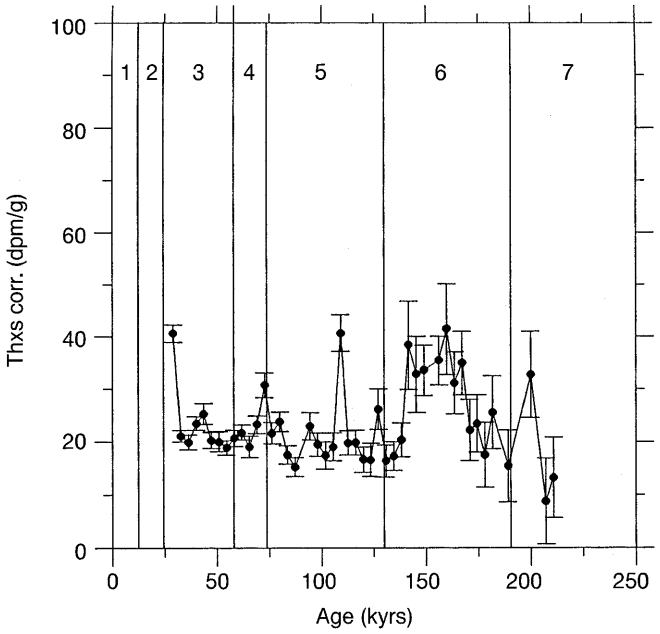

Fig. 7 Time-corrected $^{230}Th_{excess}$ profile (α-data) plotted vs age calculated with a growth rate of 110 mm/Ma. Because the manganese content (MnO_2) of nodule 63KG is up to 80 wt%, the $^{230}Th_{excess}$ data in decays per minute per gram represent the $^{230}Th_{excess}$ content per gram manganese. Assuming a constant flux of ^{230}Th into the nodule, we conclude that the maxima of ^{230}Th reflect a reduced flux of manganese into the nodule

$^{230}Th_{excess}$ activity (and thus of $^{230}Th_{excess}$ content per gram Mn) suggest a lower flux of manganese during these glacials because manganese is the main diluting component with values between 60 and 80% weight MnO_2. From the average values we can roughly estimate that the flux of Mn during stage 6 was a factor of approximately two smaller than during interglacials.

Although nodule 63KG has significantly higher levels of Mn than sediments, because it consists mainly of Mn supplied from the sediments, it is interesting to compare the profile of Mn/Fe against time in the nodule (Fig. 6) with profiles of adjacent sediment cores from the MANOP site H (Finney et al. 1988), sediments north of Galapagos (Mangini et al. 1994) and cores from the Central and Northern Peru basin (Stoffers et al. 1984) (Table 4). Sediments from these localities all display significantly higher Mn/Al ratios than average modern pelagic sediments of 0.06 (Chester and Aston 1976) probably reflecting the supply of hydrothermal Mn (except stages 2 and 3 in cores from the Galapagos Islands). This additional supply of Mn results in Mn/Fe ratios significantly higher than the average of 0.13 for modern pelagic sediments (Chester and Aston 1976).

The depth profiles of the Mn/Fe ratios in three cores from the MANOP site H (Fig. 8), located north of the Peru basin, show higher values in interglacial stages 5 and 7 than in glacial stages 4 and 6 (Finney et al. 1988). In stage 6 the Mn/Fe ratio comes close to the value of 0.13 of the detrital component. A similar trend was also observed in cores from the Galapagos Islands with a smaller or negligible hydrothermal component during stages 2 and 3 (Mangini et al. 1994).

As can be seen in Figs. 6 and 8 the nodule and the sediments display a synchronous trend in the variability of the Mn/Fe ratios. This synchronism allows us to draw further conclusions: The variability was either caused by a diminished supply of Mn to the sediments during glacials, which resulted in a diminished Mn incorporation into the nodule, or it was due to export of the remobilized Mn from the sediments to more remote areas.

The first situation implies that less hydrothermal Mn was supplied to these areas at certain times, either because the residence time of Mn in the water column changed drastically, or because the intensity of the hydrothermal source varried throughout time and/or the flow of deep water circulation altered the direction of the hydrothermal plume. If this is the case, and because post-depositional remobilization of Mn in the nodule can be ignored, the trends observed in the sediments reflect to a larger extent changes in the Mn supply, and are to a minor extent caused by diagenetic redistribution of Mn in the sediments. This interpretation is in contradiction to the general explanation of the observed variability of the profiles of Mn (or Mn/Fe) in sediments (Finney et al. 1988).

The second interpretation of the minima of Mn in sediments assumes a constant supply of hydrothermal

Table 4 Mn/Al and Mn/Fe ratios of sediment cores from different sites close to the Peru Basin and the average ratios for pelagic sediments

Location	Author	Mn/Al	Mn/Fe
MANOP site H, 6°33′N, 92°49′W	Finney et al. (1988)	0.2–0.5	0.085–0.81
Central and northern Peru basin	Stoffers et al. (1984)	0.1–0.6	0.10–0.41
Galapagos microplate (1°30′N, 102°04′W)	Mangini et al. (1994)	0.05–0.8	0.02–0.25
Average pelagic sediments	Chester and Aston (1976)	0.06	0.13

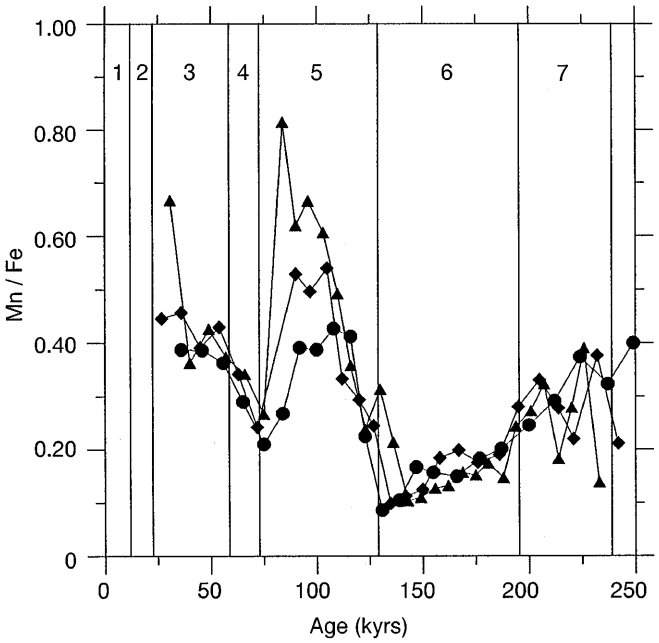

Fig. 8 Mn/Fe ratio of three sediment cores from MANOP site H (Finney 1988) plotted vs age. The *vertical lines* represent the transitions of the isotopic stages following Martinson et al. (1987). The higher ratios of Mn/Fe during interglacials and the lower values during glacials suggest that the observed variations are related to climate

Mn to sediments together with periods of strong diagenetic remobilization resulting in a higher flux of diagenetic Mn to the water/sediment interface (Dymond et al. 1984). Because periods of loss of Mn from the sediments (i.e. low Mn/Fe ratios) do not correspond with sections of faster nodule growth (higher Mn incorporation and Mn/Fe ratios), the latter implies that during glacial periods the nodule was located, at least part of the time, deeper than the redoxcline, where eventually oxidation of Mn occurs, and suboxic conditions prevented Mn precipitation. This could be an indication that suboxic conditions prevailed at least periodically at the water/sediment interface during those periods characterized by low Mn/Fe ratios in sediments. Similar evidence was derived from Mn/Fe profiles in cores from north of Galapagos (Mangini et al. 1994). Future work on other nodules and sediment samples from the Peru basin should help to decide which is the better explanation for these observations.

Conclusions

The alpha and TIMS measurements are in very good agreement. Thus, we are now able to measure into older sections of the nodule with lower ^{230}Th concentrations. In addition, TIMS yields precise ratios of the uranium activity ratio and of ^{232}Th, which might allow to better distinguish sections of different growth pattern.

Our results suggest a dependence of the manganese to iron ratio from climate in nodule 63KG because we have higher ratios during interglacials 5 and 7 as compared with glacials 4 and 6. The comparison with profiles of Mn/Fe ratios in adjacent sediments suggests that the supply of hydrothermal Mn to the sediments changed in the past. Possible explanations include (a) a variation in the intensity of the hydrothermal source, (b) a variation in the direction and/or the intensity of deep water currents and thus the hydrothermal plume and (c) a change in the residence time of Mn in the water column due to different degrees of ventilation in the deep ocean. Also, the observed low Mn/Fe ratios may be related to an enhanced export of Mn during glacial stages due to changes in the depth of the redoxcline.

References

Berger WH, Finkel RC, Killingley JS, Marchig V (1983) Glacial-Holocene transition in deep sea sediments: Manganese spike in the East-Equatorial Pacific. Nature 303:231–233

Berner RA (1980) Early diagenesis. A theoretical approach. Princeton University Press, Princeton, New Jersey

Bischoff JL, Piper DZ (eds) (1979) Marine geology and oceanography of the Pacific manganese nodule province. Marine science, vol 9. Plenum Press, New York

Boudreau BP, Scott MR (1978) A model for the diffusion-controlled growth of deep-sea manganese nodules. Am J Sci 278:903–929

Broecker WS, Peng TH (1982) Tracers in the sea. A publication of the Lamont-Doherty Geological Observatory, Columbia University, Palisades, New York,

Calvert SE, Piper DZ (1984) Geochemistry of ferromanganese nodules from domes site A, northern equatorial Pacific: multiple diagenetic metal sources in the deep sea. Geochim Cosmochim Acta 48:1913–1928

Chabaux F, Cohen AS, O'Nions RK, Hein JR (1995) ^{238}U- ^{234}U-^{230}Th chronometry of Fe–Mn crusts: growth processes and recovery of thorium isotopic ratios of seawater. Geochim Cosmochim Acta 59:633–638

Chen JH, Edwards RL, Wasserburg GJ (1986) ^{238}U, ^{234}U, and ^{232}Th in seawater. Earth Planet Sci Lett 80:241–251

Chester R, Aston SR (1976) The geochemistry of deep sea sediments. In: Riley JP, Chester R (eds) Chemical oceanography, vol. 6. Academic Press, New York

Dymond J, Lyle M, Finney B, Piper DZ, Murphy K, Conard R, Pisias N (1984) Ferromanganese nodules from MANOP site H, S, and R-control of mineralogical and chemical composition by multiple accretionary processes. Geochim Cosmochim Acta 48:931–949

Edwards RL, Chen JH, Wasserburg GJ (1987) ^{238}U- ^{234}U- ^{230}Th and ^{232}Th systematics and the precise measurements of time over the past 500000 years. Earth Planet Sci Lett 81:175–192

Edwards RL, Beck JW, Burr GS, Donahue DJ, Chappel JMA, Bloom AL, Druffel ERM, Taylor FW (1993) A large drop in atmospheric ^{14}C/^{12}C and reduced melting in the younger dryas, documented with ^{230}Th ages of corals. Science 260:962–967

Eisenhauer A, Gögen K, Pernicka E, Mangini A (1992) Climatic influences on the growth rates of Mn crusts during the Late Quaternary. Earth Planet Sci Lett 109:25–36

Finney BP, Heath GR, Lyle M (1984) Growth rates of mangneserich nodules at MANOP site H (eastern North Pacific). Geochim Cosmochim Acta 48:911–919

Finney BP, Lyle MW, Heath GR (1988) Sedimentation at MANOP site H (eastern equatorial Pacific) over the Past 400000 years: climatically induced redox variations and their effects on transition metal cycling. Paleoceanography 3:169–189

Froelich PN, Klinkhammer GP, Bender ML, Luedtke NA, Heath GR, Cullen D, Dauphin P, Hammond D, Hartmann B, Maynard V (1979) Early oxidation of organic matter in pelagic sediments of the eastern equatorial Atlantic: suboxic diagenesis. Geochim Cosmochim Acta 43:1075–1090

Halbach P, Puteanus D (1988) Geochemical trends of different genetic types of nodules and crusts. In: Halbach P, Friedrich G, Stackelberg U von (eds) The manganese nodule belt of the Pacific Ocean. Geological environment, nodule formation, and mining aspects. Ferdinand Enke Verlag, Stuttgart, pp 61–69

Halbach P, Friedrich G, Stackelberg U von (eds) (1988) The manganese nodule belt of the Pacific Ocean. Geological environment, nodule formation, and mining aspects. Ferdinand Enke Verlag, Stuttgart

Holland HD (1984) The chemical evolution of the atmosphere and oceans. Princeton University Press, Princeton, New Jersey

Huh CA, Ku TL (1984) Radiochemical observations on manganese nodules from three sedimentary environments in the North Pacific. Geochim Cosmochim Acta 48:951–963

Krishnaswami S, Mangini A, Thomas JH, Sharma P, Cochran JK, Turekian KK, Parker PD (1982) ^{10}Be and Th isotopes in manganese nodules and adjacent sediments: nodule growth histories and nuclide behavior. Earth Planet Sci Lett 59:217–234

Ku TL, Broecker WS (1967) Uranium, thorium and protactinium in an Mn nodule. Earth Planet Sci Lett 2:317–320

Leinen M, Pisias N (1984) An objective technique for determining end-member compositions and for partitioning sediments according to their sources. Geochim Cosmochim Acta 48:47–62

Lyle M (1981) Formation and growth of ferromanganese oxides on the Nazca plate. Geol Soc Am Mem 154:269–295

Lyle M, Heath RG, Pisias NG (1979) Sedimentation at MANOP site S, 11°N, 140 W, Central Pacific Ocean. EOS 60:850

Mangini A (1988) Ages and growth rates of Mn nodules and crusts. In: Halbach P, Friedrich G, Stackelberg U von (eds) The manganese nodule belt of the Pacific Ocean. Geological environment, nodule formation, and mining aspects. Ferdinand Enke Verlag, Stuttgart, pp 142–151

Mangini A, Eisenhauer A, Walter P (1990) Response of manganese in the ocean to the climatic cycles in the Quaternary. Paleoceanography 5:811–821

Mangini A, Rutsch HJ, Frank M, Eisenhauer A, Eckhardt JD (1994) Is there a relationship between atmospheric CO_2 and manganese in the ocean? NATO ASI Ser 117:87–104

Martinson DG, Pisias NG, Hays JD, Imbrie J, Moore TC Jr, Shackleton NJ (1987) Age dating and the orbital theory of the Ice Ages: development of a high-resolution 0 to 300000-year chronostratigraphy. Quaternary Res 27:1–29

Puteanus D, Glasby GP, Stoffers P, Mangini A, Kunzendorf H (1989) Distribution, internal structure and composition of manganese crusts from the seamounts east of the Teahitio-Mehetia Hot Spot, Southwest Pacific. Marine Mining 8:245–266

Reyss JL, Marchig V, Ku T (1982) Rapid growth of a deep-sea manganese nodule. Nature 295:401–403

Schmitz W (1985) Sedimentverteilung und Akkumulationsraten im S.W. Pazifischen Becken (Transekt Tahiti – Ostpazifischer Rücken – Neuseeland, entlang 42°S). Dissertation, Universität Heidelberg

Segl M, Mangini A, Beer J, Bonani G, Suter M, Wölfli W (1989) Growth rate variations of manganese nodules and crusts induced by paleoceanographic events. Paleoceanography 4:511–530

Stackelberg U von (1988) Principles of nodule field formation. In: Halbach P, Friedrich G, Stackelberg U von (eds) The manganese nodule belt of the Pacific Ocean. Geological environment, nodule formation, and mining aspects. Ferdinand Enke Verlag, Stuttgart, pp 159–166

Stoffers P, Sioulas A, Glasby GP, Schmitz W, Mangini A (1984) Sediments and micronodules in the Northern and Central Peru Basin. Geol Rundschau 73:1055–1080

Walter P, Stoffers P (1985) Chemical characteristics of metalliferous sediments from eight areas on the Galapagos Rift and East Pacific Rise between 2°N and 42°S. Mar Geol 65:271–287

Weiss RF (1977) Hydrothermal manganese in the deep sea: scavenging, residence time, and Mn/^{3}He Relationships. Earth Planet Sci Lett 37:257–262